A Step Toward Control of the Surface Structure of Biomimetic Hydroxyapatite Nanoparticles: Effect of Carboxylates on the {010} P-rich/Ca-rich Facets Ratio

UNIVERSITÀ DEGLI STUDI DI TORINO

A Step Toward Control of the Surface Structure of Biomimetic Hydroxyapatite Nanoparticles: Effect of Carboxylates on the {010} P-rich/Ca-rich Facets Ratio

Yuriy Sakhno,[a*] *Pavlo Ivanchenko,*[a] *Michele Iafisco,*[b] *Anna Tampieri,*[b] *Gianmario Martra* [a*]

ABSTRACT

Two types of biomimetic hydroxyapatite (HA) nanoparticles were prepared by acid-base neutralization reactions, using $Ca(OH)_2$ or $Ca(CH_3COO)_2$ as s calcium source, to evaluate the effect of acetate anions on particle formation. High-resolution transmission electron microscopy observations provided evidence that in both cases, nanoparticles are elongated along the c-axis, but to a more limited extent when prepared in the presence of acetates, and are mainly limited by {010} facets. IR spectra of nanoparticles containing adsorbed CO revealed that the actual termination of these are both of the {010}_Ca–rich and {010}_P–rich type, the latter being significantly more abundant for HA nanoparticles grown in the medium containing CH_3COO^- species. Moreover, these nanoparticles appeared to be more sensitive toward aggregative stacking by thermal treatment, resulting in a significant decrease in specific surface area, while retaining the size of primary particles.

1. INTRODUCTION

Hydroxyapatite (HA), [$Ca_{10}(PO_4)_6(OH)_2$], the calcium phosphate phase thermodynamically stable in physiological environment, is nowadays considered an important bioactive and bioresorbable biomaterial for applications in orthopaedy and dentistry.[1-3] In particular, since the group of Webster reported about the beneficial effect of hydroxyapatite nanosizing in improving the response elicited in osteoblasts[4] several research works have been devoted to the disclosure of preparation routes for the production of nano-hydroxyapatites. The surface of biomaterials plays a significant functional role, further enhanced when they are in a nanosize form, because it is the place where the interaction with host biological media occurs, as recognized since the definition of the concept of biological/biomedical surface science.[5-7] Moreover, nano-HA have raised an increasing interest as heterogeneous catalysts,[8-9] another functionality mainly ruled by surface features.

Focusing on nano-HA morphology, needle-like[10-13a] and plate-like,[13b,14] nanoparticles can be prepared, while in bone tissue only the second type seems to be present.[15-17] For both morphologies the prevailing surface terminations are of the {010} type, which in the case of needle-like nano-HA are the lateral facets of hexagonal nanoparticles elongated along the crystallographic c-axis, whilst for plate-like nanoparticles they are the basal facets of nanoparticles preferentially grown along both the c- and a- (or b-) axis,[14,18] breaking the crystal symmetry through a mechanism still matter of investigation.[13b,18]

The role of different surface crystal planes when considering the interaction of HA with biomolecules has been initially recognized by Kandori et al., who demonstrated that basic proteins are mainly adsorbed on HA {001} faces, whereas the acidic ones preferentially interacts with HA {010} surfaces.[19] This latter type of surfaces can be thought as resulting from the interruption of a sequence of layers of the ...A–B–A–A–B–A–A–B–A–... type, where A and B correspond to $Ca_3(PO_4)_2$ and $Ca_4(PO_4)_2(OH)_2$ chemical compositions, respectively. Hence, a {010} surface termination of the ... –A–B–A type give origin to stoichiometric HA{010} surfaces, whilst ...

–A–A–B, or ... –B–A–A types result in two nonstoichiometric HA{010} facets, labelled as (010)_Ca-rich and (010)_P-rich, respectively. The coexistence of these non-stoichiometric surfaces on HA particles was reported also by Sato et al.[20] and by Ospina et al..[21] Moreover, theoretical calculations indicated that the HA {010} stoichiometric surface reacts spontaneously with water,[22-23] generating P-OH and new Ca-OH surface hydroxyl groups, resulting in {010} facets labelled as {010}R (R="reacted"). A pictorial overview of all these types of {010} terminations is displayed in Scheme 1.

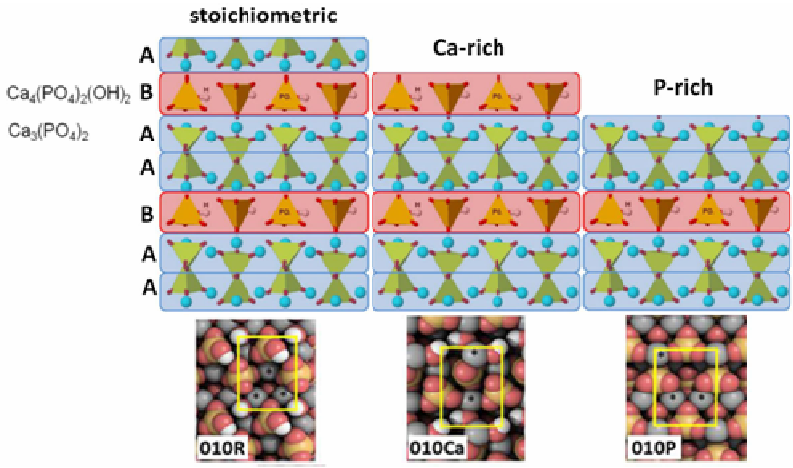

Scheme 1. Upper part: side view of the sequence of A) $Ca_3(PO_4)_2$ and B) $Ca_4(PO_4)_2(OH)_2$ layers in the bulk structure of HA along the cross section perpendicular to the (010) surface. Bottom part: top view of the three possible (010) terminations (see text for details). The upper part is a courtesy by Dr. F. Chiatti, PhD Thesis, Torino, 2014; the bottom part is adapted from ref.[24]

Despite experimental evidence of the exposure of these terminations can be provided by HR-TEM,[20-21] the occurrence of proper orientation and stability of HA nanoparticles under the electron beam in order to observe so subtle differences is not an obvious task. Conversely, the use of probe molecules does not usually suffer of relevant limitations, and IR spectroscopy of adsorbed CO has been already used to investigate the Lewis acidity of Ca^{2+} ions exposed at the surface of HA nanoparticles, (14a,b; [25]) as well as the influence of Mg^{2+} substitution on the basic properties of HA[26] and features of surface hydroxy groups.[27] In this respect, Chiatti et al. reported that the spectra of adsorbed CO can be exploited to evaluate the relative contribution of (001) and three types of

(010) terminations to the surface of HA nanoparticles.[24] This was the basis of the present study, aimed to the evaluation of the effects of the presence of carboxylate anions in the synthesis medium on textural and surface features of HA nanoparticles. In particular, acetates were considered, as calcium acetate is among the possible source of Ca^{2+} ions in HA synthesis. [28-29] The interest towards the action of carboxylate groups stems from the increasing awareness of their role in addressing chemical, structural and textural properties of hydroxyapatite.[30-34] Indeed, this is a bio-inspired approach, which aim to mimic the apatite formation mechanisms that occurred in nature, since it is well-known that nucleation and/or growth of bone crystals is regulated by acidic functional macromolecules, such as bone sialoprotein[35-36] and osteopontin[37] as well as small acidic molecules, such as citrate, which, in particular, was found to stabilize size and morphology of bone apatite [38-39] Turning to synthetic apatites, citrate were found to inhibit apatite crystal growth by strongly interacting with the surface,[40] and very recently were proposed to play an important role in driving the bio-inspired formation of platy apatite nanocrystals.[18]

Furthermore, it was reported that amino acids can bind preferentially to specific HA crystal face and inhibit growth in the direction perpendicular to that face.[41-42]_ENREF_44 Thus, on one hand they can be viewed as shape controller of HA nanoparticles, but, on the other hand, amino acids amino acids were also found to increase the bioactivity of synthetic HA.[43-45] At the best of our knowledge, in all these cases the effects of carboxylates bearing molecules on the structure on HA surfaces formed in the presence of these agents was not investigated, including the research works on HA prepared by using $Ca(CH_3COO)_2$, where, for instance, the attention was focused on the relative importance of stoichiometry-non-stoichiometry vs structural order–disorder in determining structural feature of nano-HA.[28] Hence, this paper is intended as a contribution to the knowledge of factor which can affect the structure of the most abundantly exposed surface termination of HA nanoparticles.

2. EXPERIMENTAL

2.1. Materials

Two types of HA nanoparticles were prepared using a similar procedure (i.e. similar Ca/P ratio of reactants, pH of reaction medium and temperature), but changing the source of calcium ions, namely $Ca(OH)_2$ and $Ca(CH_3COO)_2$, resulting in materials hereafter referred to as HA–1 and HA–2, respectively. For the preparation of HA–1, an H_3PO_4 solution (1.26 M, 0.6 L) was dropped into a $Ca(OH)_2$ suspension (1.35 M, 1 L) and kept at 310 K, to accomplish the following theoretical reaction:

$$5Ca(OH)_2 + 3H_3PO_4 \rightarrow Ca_5(PO_4)_3OH + 9H_2O$$

HA–2 was prepared by dropping the H_3PO_4 solution (0.21 M, 0.8 L) into a $Ca(CH_3COO)_2$ solution (0.35 M, 0.8 L), kept at 310 K as in the previous case, and pH of approximately 10 by addition of NH_4OH solution, resulting in the occurrence of the following theoretical reaction:

$$5Ca(CH_3COO)_2 + 3H_3PO_4 + 10NH_4OH \rightarrow Ca_5(PO_4)_3OH + 10CH_3COOH + 9H_2O + 10NH_3$$

In both cases reaction mixtures were stirred overnight. The stirring was then stopped and mixtures were left standing for 2 hours to allow for deposition of the inorganic phase. HA powders were then isolated by centrifugation of the mother liquor, repeatedly washed with water and dried at 213 K under outgassing (residual pressure: 3 mbar) overnight. HA granular fractions having dimensions <38 μm (400 mesh) were selected for the study by sieving the powder. For IR measurements, H_2O and D_2O (99.9 atom % D, Aldrich) were admitted onto the samples after several freeze-pump-thaw cycles, whereas high-purity CO (Praxair) was employed without any additional purification except liquid nitrogen trapping.

2.2. Methods

Specific surface area (SSA) was measured with a Micromeritics ASAP 2010 by nitrogen adsorption at 77 K following the BET model. Before measurements, as-prepared materials were outgassed at 300 K for 10 h (allowing for the attainment of a residual pressure of $1 \cdot 10^{-3}$ mbar), while samples otherwise treated in vacuum at 433 and 573 K were re-outgassed at this temperature.

The Ca/P ratio was determined by inductively coupled plasma-optical emission spectrometry (ICP-OES, Liberty 200, Varian). Samples were dissolved in 1% wt ultrapure nitric acid. The analytical wavelengths chosen were 422 nm for Ca and 213 nm for P.

The carbonate content was evaluated on dried samples by thermogravimetric analysis (TGA) using a Thermal Analysis SDT Q 600 (TA Instruments) according to the weight loss observed between 673 and 1223 K.[46] Heating was performed under a nitrogen flow (100 ml min^{-1}) using an alumina sample holder at a rate of 10 K min^{-1} up to 1473 K. The weight of the samples was approximately 5 mg.

X-ray diffraction (XRD) patterns of the powders were recorded with an Analytical X'Pert Pro equipped with an X'Celerator detector powder diffractometer using Cu Ka radiation generated at 40 kV and 40 mA. The instrument was configured with 1/2° divergence and receiving slits. A quartz sample holder was used. The 2θ range was from 5° to 60° with a step size (°2θ) of 0.05 and a counting time of 3 s.

The degree of HA crystallinity was calculated according to the formula (1):

$$\text{Crystallinity (\%)} = [C/(A+C)] \cdot 100 \qquad (1)$$

where C was the area of the peaks in the diffraction pattern ("the crystalline area") and A was the area between the peaks and the background ("the amorphous area").

Crystal domain size along the HA axis directions were calculated applying the Scherrer equation (2):

$$L_{hkl} = 0.94\lambda \cdot [\cos\theta \cdot (\Delta r^2 - \Delta_0^2)^{1/2}] \qquad (2)$$

where θ is the diffraction angle for the plane (hkl), Δr and Δ_0 the widths in radians of reflection hkl at half height for the synthesized and pure inorganic hydroxyapatite (standard reference material, calcium hydroxyapatite, National Institute of Standards & Technology), respectively, and λ=1.5405 Å.

High-resolution transmission electron microscopy (HR–TEM) images of the materials (powder grains dispersed on Cu grids coated with a lacey carbon film) were obtained with a JEOL 3010-UHR operated at an acceleration potential of 300 kV. As apatite samples might evolve under the electron beam, potentially leading to further crystallization and/or to a loss of bulk water,[47-49] observations were conducted under feeble illumination conditions to avoid any modification of the materials during the analysis. Fourier Transforms of direct images were performed using the Gatan Digital Micrograph program software.

For IR studies, the powders were pressed into self-supporting pellets and placed in quartz IR cells designed to perform spectroscopic measurements both at beam temperature (b.t., ca. 323 K; cell equipped with CaF_2 windows) or at low temperature (ca. 100 K, by cooling with liquid N_2; cell equipped with KBr windows). The cell was connected to a conventional vacuum line (residual pressure = 1×10^{-5} mbar, 1 mbar = 100 Pa) to perform in situ all thermal treatments and adsorption-desorption experiments. The spectra were collected at a resolution of 4 cm^{-1} with a Bruker Vector 22 spectrometer, equipped with a DTGS detector. The number of scans was adjusted from 150 to 250 to attain a good signal-to-noise ratio. Each set of measurements was carried out on three different samples of each material. The data were normalized to the intensity of a pattern in the 2200-1900 cm^{-1} range due to a combination and overtone of vibrational modes of bulk phosphate groups in order to render differences in intensity independent of differences in the thickness of the

pellets. For comparative analysis of the intensity of surface species, some spectra were also normalized with respect to the SSA.

Spectra of adsorbed CO are reported in Absorbance, after subtraction of the spectra of the sample before CO admission. Moreover, the spectrum of gaseous CO was subtracted from the spectra of the samples collected in the presence of CO equilibrium pressures ranging from 25 to 4 mbar, with a proper adjustment of the intensity using the interactive spectrum subtraction utility of the OPUS 5.0 software by Bruker. For lower CO equilibrium pressures, the high SSA of the materials (see Table 1) resulted in an overwhelming intensity of the spectral components due to adsorbed CO with respect to the roto-vibrational profile of CO molecules in gas phase. A comparison between spectra of adsorbed CO before and after subtraction of the contribution of gaseous CO in equilibrium with the sample is displayed in the left panel of Figure S7 in the Supporting Information, hereafter SI, where all complementary data dealing with experimental IR spectra of adsorbed CO are reported.

IR spectra of adsorbed CO were fitted accordingly to the procedure reported in ref.[24] In summary, for each structure *i* of carbonyl adducts (containing from 1 to 4 CO molecules) computed in that work, the CO stretching IR spectrum $S_i(\nu)$ was computed as a linear combination of Gaussian functions $G(\nu - \nu_j)$, each one centered at the *j*th CO B3LYP rescaled frequency value ν_j, and a 15 cm^{-1} full width at half-maximum (FWHM), weighted by the corresponding calculated IR intensity (I_j)

$$S_i(\nu) = \sum_j I_j \cdot G(\nu - \nu_j)$$

Hence, at this level, the only guess was the FWHM value adopted, which was consistent with the FWHM = 15 cm^{-1} of the νCO band at very low CO coverage, where only monocarbonyls, producing a single band, should be overwhelmingly present.

A linear combination $T(\nu)$ of all the computed $S_i(\nu)$ spectra represents the resulting spectrum in which, however, the weights w_i of each $S_i(\nu)$ have to be, somehow, determined

$$T(\nu) = \sum_i w_i \cdot S_i(\nu)$$

The criterion adopted to choose the weights w_i has been to run a nonlinear regression between the experimental IR spectrum and the computed $T(\nu)$ one, by keeping constant the relative ratios of the computed I_j intensities within the same case i, while changing their absolute values.

The analyses were performed three times on the same synthesis product. Data from SSA, ICP, TGA, and XRD are presented as mean value ± standard deviation.

3. RESULTS AND DISCUSSIONS

3.1. Compositional and textural features

Codes, composition, and specific surface area (SSA) of the investigated materials are listed in Table 1. For both samples, the Ca/P ratio was slightly lower than the stoichiometric one (1.67), and a limited amount of carbonate groups, derived from unintentionally dissolved CO_2 in the preparation media and from CO_2 adsorbed onto the surface materials during the storage, was present.

Table 1. Codes, compositional features (Ca/P ratio, carbonate content), specific surface area (SSA_{BET}), average size of crystal domains along the [002] and [310] directions and degree of crystallinity of the two HA materials.

Materials	Bulk Ca/P (mol)	Carbonate species (wt%)	SSA_{BET} ($m^2 \cdot g^{-1}$)		D002 (nm)[a]	D310 (nm)[a]	Degree of crystallinity (%)
			materials as prepared and outgassed at 433 K	materials outgassed at 573 K			
HA–1	1.65±0.2	1.0±0.1	130 ±6	120 ± 6	37 ± 5	9 ±3	72% ± 3
HA–2	1.62±0.2	1.8±0.2	160 ±10	90 ±5	22 ± 4	7 ± 3	60% ± 3

[a] obtained by applying the Scherrer equation

In the as-prepared form, HA–1 exhibited a ca. 20% lower SSA than HA–2, in agreement with the reverse order of nanometric size observed by TEM (see next section), and the same values were obtained after outgassing the materials at 433 K. Conversely, in the case of HA–2, thermal treatment up to 573 K resulted in a significant decrease (ca. 45%) of SSA, which decreased less than 10% for HA–1.

General structural insights were obtained from the XRD patterns (Figure 1), characterized by quite broad diffraction peaks located at 2θ values characteristic of a hydroxyapatite single phase (JCPDS 9-432). Using formula (1) reported above, degrees of crystallinity of 72% ± 3 and 60% ± 3 (difference statistically significant: p-value < 0.0001) for HA–1 and HA–2, respectively, were found. Furthermore, in both cases, an elongation of the coherent scattering (crystalline) domains along the c–axis of the HA hexagonal structure (data dealing with the [002] direction in Table 1) were obtained, although more limited for HA–2. Finally, essentially the same XRD patterns were obtained for the material treated at 573 K (see Figure S1 in the SI). The lower degree of crystallinity of HA-2 might result from the larger content in carbonate species of this materials, because larger amounts of substituent species in the bulk/larger deviation from stoichiometry contribute to the shortening of the coherency domains.

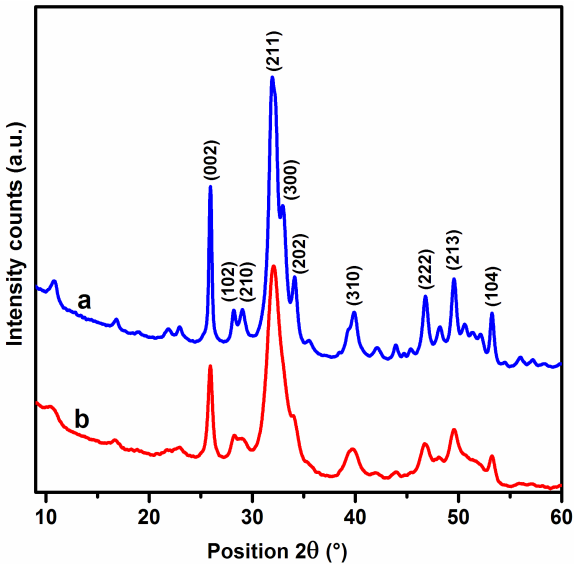

Figure 1. XRD patterns of: a) HA–1 and b) HA–2. Diffraction peaks assigned on the basis of JCPDS 9-432.

3. 2. Structural and morphological characterization

Complementary structural and dimensional investigations were performed by HR-TEM observations. Low magnification images representative of the size and morphology of the particles constituting the two materials are displayed in Figure 2.

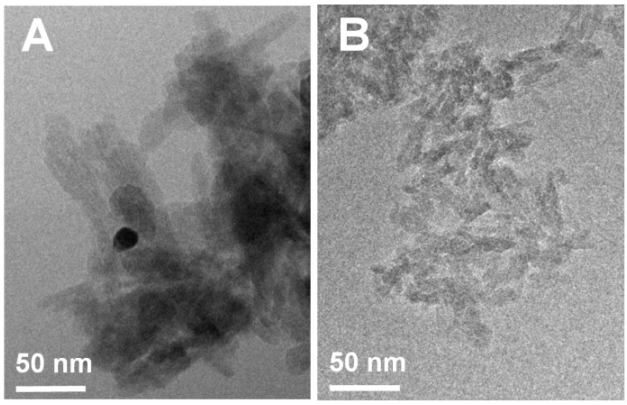

Figure 2. TEM images representative of the size and morphology of: A) HA–1 and B) HA–2.

In the case of HA–1, a significant portion of particles appeared projected on the image plane (it is worthy to remember that TEM images are 2D representation of 3D objects) as a needle-like shape, with sizes (length × width) of ca. 40–70 × 5–10 nm (panel A). Interestingly, a few roundish shapes, ca. 10 nm in diameter, were also present, exhibiting a much higher contrast. Taking into consideration that at low magnification the only effective contrast mechanism is the mass-thickness mechanism,[50] such roundish shapes likely resulted from the projection in the image plane of needle-like particles viewed along their major axis *c*. Following TEM imaging of HA–2, mainly rectangular shapes with sizes (length × width) of ca. 30 × 5–10 nm and 30 × 10–15 nm, were observed (panel B), indicating that this material was composed of smaller (in particular, shorter) nanoparticles, in agreement with the slightly larger SSA (see Table 1). After outgassing up to 573 K (treatment required for the IR study, see below), the primary particles of both materials essentially retained their original size and shape (Figure S2 in SI). Hence, the decrease in SSA resulting from such treatment (see Table 1) might be ascribed to a stacking-like particle aggregation, occurring to a large extent in the case of HA–2. At higher magnifications (Figure 3), lattice fringes were observed,

and their orientation with respect to the borders provided insights on the crystallographic features of the particles.

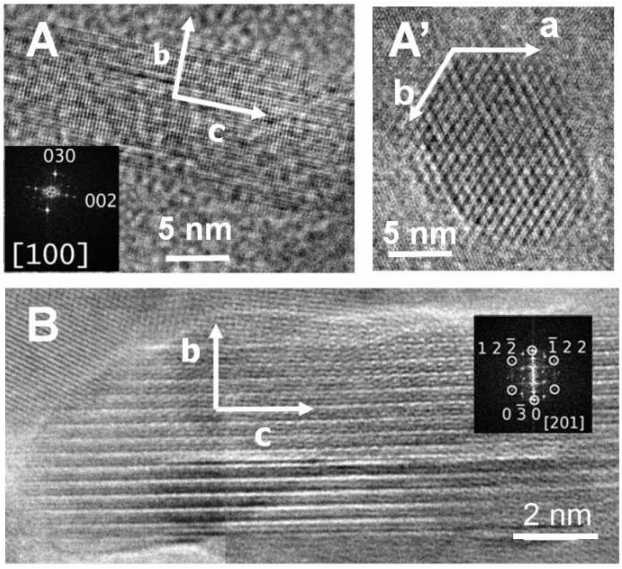

Figure 3. HR–TEM images of HA nanoparticles. HA–1 : panel A, side view of a particle, and related FT; panel A', cross-sectional view of a particle. HA–2: panel B, side view of a particle, and related FT.

Indeed, HA–1 nanoparticles were elongated towards the c-axis (Figure 3A), whereas cross-sectional views (particles oriented with the c-axis parallel to the electron beam/line of observation) revealed that facets parallel to such axes are of the (010) type (Figure 3A'). Similar features were observed in the case of HA–2 particles, which exhibited the same type of facets, but appeared less elongated toward the c-axis (Figure 3B; note that in this figure, the b-axis lies in the image plane, whereas a ca. 20° angle exists between the latter and the c-axis: particle view along the [201] zone axis). Essentially, it can be inferred that the presence of acetate anions in the preparation medium limited the growth of HA–2 nanoparticles along the c-axis, which is in agreement with the findings of Puvvada et al.[51]

Finally, it must be noted that HR–TEM and XRD data agree in providing evidence of the elongation of nanoparticles, whereas particle sizes obtained by TEM appeared to be larger than crystal domains observed by XRD (Table 1). Such a discrepancy stems from the fact that i)

polycrystalline particles might be present, and ii) TEM allows the determination only of ranges of values, whereas by XRD average values are obtained.

3.3. Surface features of the "as-prepared" materials: hydration state and carbonate groups

Figure 4 shows the patterns representative of the IR spectra of the materials in contact with 20 mbar of H_2O vapor (curve a), outgassed at beam temperature (b.t.; curve b), and after the final outgassing at the end of a series of D_2O adsorption/desorption cycles (curve c). In particular, the data displayed were obtained for HA–2, while the equivalent data collected for HA–1 are reported in Figure S3 in SI.

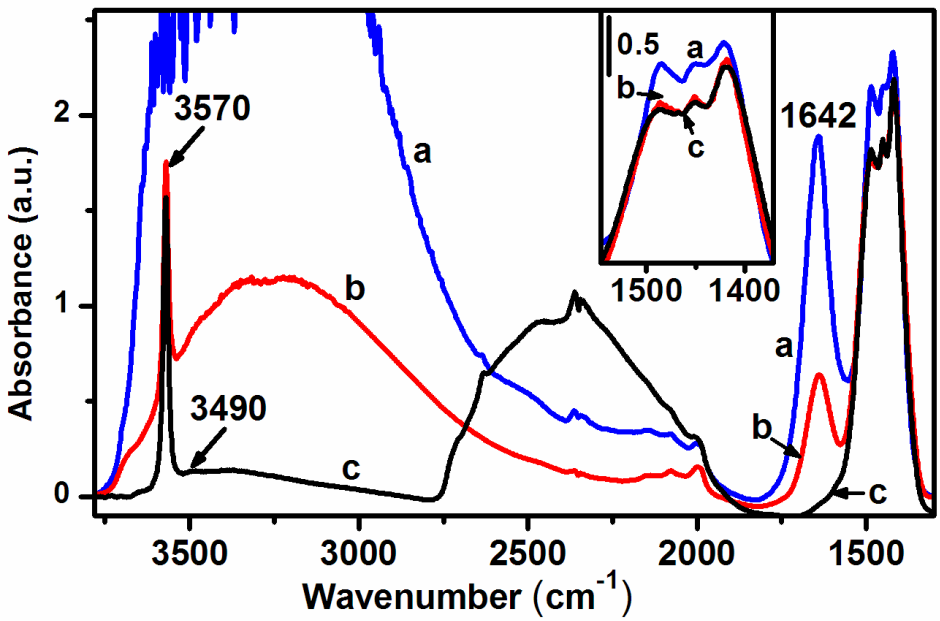

Figure 4. IR spectra of HA–2: (a) in the presence of 20 mbar of H_2O, (b) after 60 min outgassing at b.t., (c) after exchange with D_2O and subsequent 60 min outgassing at b.t.. Inset: zoom of the carbonate νCO region.

Table 2. General assignment of the bands present in the IR spectra (3800-1350 cm^{-1} range) of nano–HA in contact with 20 mbar of H_2O, after 60 min outgassing at b.t., and after exchange with D_2O and subsequent outgassing at b.t..[14]

Band position (cm^{-1})	**Assignments**
3800-2500 (range)	stretching modes of adsorbed H_2O, bulk and surface hydroxy groups (e.g. of HPO_4^{2-}) involved in H-bonding
3570 (centre of a narrow band)	stretching mode of bulk OH^-, occupying the 4e position in the hexagonal lattice ("columnar OH", because aligned in columns parallel to the *c*-axis)
2750-2000 (range)	stretching modes of adsorbed D_2O, and surface –OD groups involved in H-bonding
2000-1900 (weak; range)	combination modes of fundamental phosphate bulk absorption (falling below the limit of transparency of the pellets used for this study)
1640 (band centre)	H_2O deformation mode (δH_2O) (shifted at ca. 1200cm^{-1} for D_2O, below the transparency limit of the materials pellettized in a self-supporting form)
1600-1370 (range)	antisymmetric stretching modes of carbonate groups

The assignment of the various signals is summarized in Table 2. Focusing on Figure 4, it can be observed that the δH_2O band (at ca. 1640 cm^{-1}) still exhibited ca. 30% of the original intensity after outgassing at b.t. (curve b), witnessing the coordination of water molecules on surface Ca^{2+} ions.[14, 23] The stretching modes of such molecules contribute to the broad absorption in the 3700-2750 cm^{-1} range, overlapping the sharp peak at 3570 cm^{-1} typical of bulk columnar OH in a 4e lattice position. The shift to lower frequency of the signals due to water molecules after H_2O/D_2O exchange (curve c) reveals the resistance to such exchange not only of the peak at 3570 cm^{-1} (expected), but also of a broad νOH band in the 3500-2750 cm^{-1} range. The absence of a δH_2O partner indicated that this feature must be assigned to bulk hydroxyl groups involved in H-bonding, likely belonging to HPO_4^{2-} species,[14] and not to entrapped water molecules.[52]

It is important to note that no signals due to acetate species, the antisymmetric νCOO^- mode which should produce a band in the 1650-1550 cm^{-1} region[53], were detected, indicating that

CH_3COO^- ions were neither entrapped in the bulk nor left adsorbed on the surface of nanoparticles. Accordingly, TGA curves did not exhibit peculiar features assignable to acetates (see Figure S4 in the SI, and related comment). Thus, the data collected indicated that these species were effectively removed during the washing procedure. Likely, they acted as weaker ligands for Ca^{2+} ions with respect to di- and tricarboxylic Ca^{2+}-chelating agents and amino acids, which typically remained associated to HA nanoparticles after washing.[13,40-45]

Moving to lower frequency, the pattern in the 1550-1370 cm^{-1} range (expanded as an inset), related to the antisymmetric stretching modes of carbonate groups[47, 54-56] appeared to be sensitive to the amount of adsorbed water (curves a, b), indicating that they were present to some extent on the surface of HA nanoparticles. To avoid any additional effect of this spectral evolution, possibly due to the low frequency tail of the δH_2O band, the response of carbonates to surface hydration was evaluated by hydrating and dehydrating the samples with D_2O, exhibiting the band due to the deformation mode at ca. 1200 cm^{-1}. The results obtained for the two materials are compared in Figure 5.

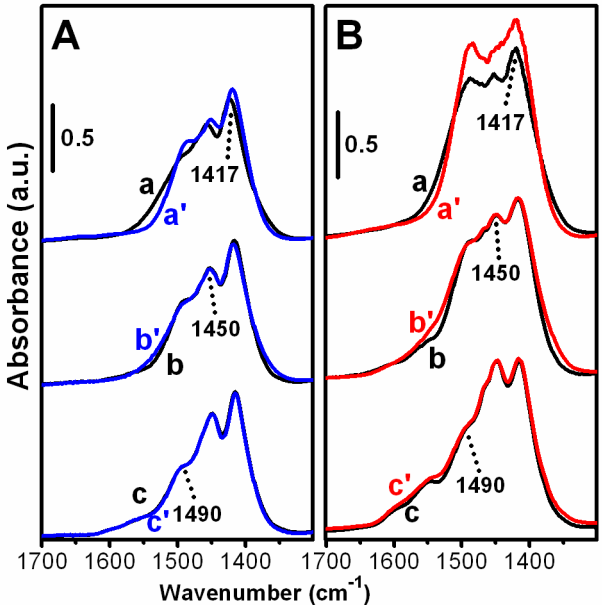

Figure 5. Spectra, in the 1600-1350 cm^{-1} range, of (A) HA–1 and (B) HA–2. Samples underwent D_2O adsorption/desorption cycles until invariance of the spectra, and then were outgassed for 60 min at: a) beam temperature, b) 433, c) 573 K. Spectra a′-c′: spectra collected in the presence of D_2O vapor (20 mbar) on the samples pre-outgassed at the indicated temperatures.

The two patterns exhibit a relative intensity consistent with the difference in carbonate content of the two materials (see Table 1); the assignment of the various components is reported in Table 3, based on the voluminous literature on IR spectroscopy of carbonate in the bulk of apatites, ranging from pioneering studies [55b,57,58] to the most recent proposals.[54]

Table 3. General assignment based on refs[54,57] of the IR pattern due to antisymmetric stretching modes of carbonates in apatites in the 1650-1400 cm^{-1} range.

Band position (cm^{-1})	**Assignment**
1600-1500 (range)	carbonates substituting columnar OH- : A-type
1500-1450 (range)	both carbonates substituting columnar OH- (A-type) and carbonates substituting phosphates (B-type)
1420-1410 (centre of a narrower band)	carbonates substituting phosphates: B-type

On such a basis, weak and unresolved features in the 1600-1500 cm^{-1} range monitor the scarce content in A-type carbonates, whereas the B-type, characterized by bands in the 1550– 1350 cm^{-1}, range should be predominant and is expected for precipitated apatites.[54,55b,57-58] The removal of D_2O multilayers from the materials in the "as-prepared" form (curves a, a' in both panels) affected to a larger extent the $\nu CO_3^{2-}{}_{asym}$ spectral pattern of HA–2, indicating that a larger amount of carbonate groups should be present on the surface of these nanoparticles. This effect significantly decreased for both materials pre-outgassed at 433 K (curves b, b' in both panels), monitoring the removal of most of the surface carbonate groups, and then disappeared following outgassing at 573 K curves c, c' in both panels), demonstrating the complete removal of surface carbonate groups. Moreover, it can be observed that the relative intensity of the various components in the 1550-1350 cm^{-1} range appeared different in the spectra of the two materials in the "as-prepared form" (curves a in both panels), and then, by increasing the treatment temperature, the spectral profile of HA–2 became progressively similar to that of HA–1, indicating the initial presence in HA–2 of B-type

carbonate with a different local structure [54] then evolving by thermal treatment towards species more similar to those present in HA−1 nanoparticles.

3.4. Amounts of surface hydroxyl groups and adsorbed H_2O molecules

The next target was the quantitative assessment of adsorbed water molecules and surface hydroxyl groups in the two materials. In this respect, spectral patterns containing only signals due to such surface species were obtained by subtracting the spectra collected after exchange with D_2O and subsequent outgassing from those recorded after outgassing at b.t. [curves (c) and (b), respectively, in Figure 4 and Figure S3 in SI]. Briefly, spectra obtained along the adopted stepwise procedure are displayed in Figure S5 in the SI, while the results of the quantitative analysis of such spectra are reported here in Table 4 and in the text below. Before the subtraction, all spectra were normalized both to the amount of sample (see the Experimental section) and to the specific surface area in order to refer to spectral intensities related to equivalent surface extensions. Hence, differences in intensity of the components obtained after the subtraction must only reflect differences in the amount of surface hydration between the two materials. The relative integrated intensities of the νOH signal (3750-2500 cm^{-1}, due to both surface hydroxyl groups and water molecules) and δH_2O (1800-1550 cm^{-1}, only due to surface water molecules) for samples outgassed at b.t. were then calculated (Table 4). A similar evaluation was performed for materials in equilibrium with 20 mbar H_2O, but limited to the δH_2O band, as the maximum of the νOH signal was out of scale.

Table 4. Relative integrated intensity (I) of the νOH band in the 3750-2500 cm^{-1} range (resulting from both hydroxy groups and H_2O molecules) and δH_2O band (1800-1550 cm^{-1}) in the spectra of HA−1 and HA−2 outgassed at b.t. for 60 min (spectral data is in Figure S5 of the SI).

	samples outgassed at b.t.					
	I **δH_2O (cm^{-1}/nm^2)**	**conversion factor**	**H_2O molecules /nm^2**	***relative I*** **δH_2O (cm^{-1})**	***relative* I*** **νOH (cm^{-1})**	***I*** **νOH / *I*** **δH_2O**
HA−1	3.3±0.3	1.3±0.1	4.3 ± 0.3	1.1± 0.2	26.4± 1.3	24.0± 3.8
HA−2	3.0±0.3	1.3±0.1	3.9 ± 0.3	1.0± 0.2	25.2± 1.3	25.2±4.1
HA from previous studies*	3.5±0.5	1.3±0.1	4.5± 0.5	1.2± 0.2	33.5± 1.7	27.9± 4.9

* with respect *I* δH_2O of HA-2 assumed as unity (second row, fifth column)
**from ref. [14]

Using the conversion factor from the integrated intensity of the δH_2O band, the number of water molecules per surface unit derived in previous studies[14] (Table 4, last row), the amounts of water molecules remaining coordinated to surface cations after outgassing at b.t. were calculated (Table 4, columns 4). It is worthwhile to note that the interaction of H_2O molecules with the surface is governed not only by the coordinative interaction with cationic sites, but also by a strong H-bonding interaction with oxygen atoms of phosphate groups, as indicated by both theoretical and experimental investigations.[59-60] The analysis of the broad signal in the 3500-2500 cm^{-1} range was less straightforward because of the superposition of the νOH components due to adsorbed water molecules and surface hydroxyl groups involved in H-bonding. Then, the ratio between the integrated area of the OH stretching band (*I* νOH), due to both hydroxyl groups and water molecules, and the δH_2O band (*I* δH_2O), due to water molecules only, was calculated. The *t* test carried out at a 95% confidence level on both H_2O/nm^2 and *I* νOH/*I* δH_2O values indicated that, in this respect, HA-1 and HA-2 materials are equivalent to another type of HA nanoparticles considered in previous studies,[14] exhibiting at their surface ca. 4.5 H_2O and 1.0 OH per nm^2.

Then, the collection of data resulting from HR−TEM observations and analysis of IR spectra of surface hydration species indicate the predominance of {010} surface terminations for both

HA–1 and HA–2 materials, where {010}R expected to expose 3 OH groups per nm^2 should be a minor fraction.[60] To investigate in more detail the types of facets actually exposed by the two materials, IR spectra of adsorbed CO were then acquired.

3.5. Surface structures as revealed by IR spectroscopy of adsorbed CO

To probe surface Ca^{2+} ions by infrared spectroscopy of adsorbed CO, H_2O molecules left irreversibly adsorbed on HA nanoparticles by outgassing at b.t. must be removed (as well as carbonates, see above) at higher temperatures.[14]

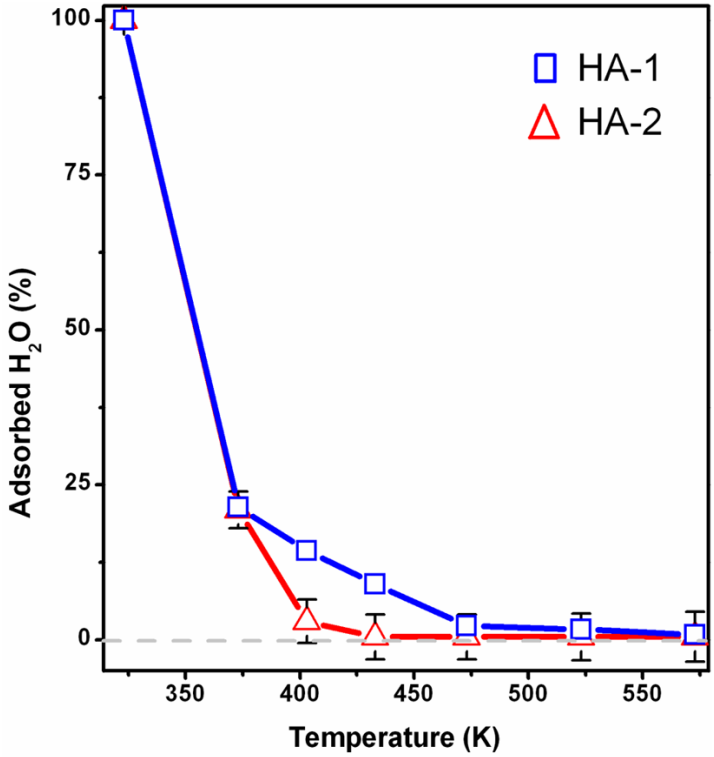

Figure 6. Relative amount of H_2O molecules left adsorbed on HA–1 (blue) and HA–2 (red) after outgassing at increasing temperature, with respect to the materials outgassed at beam temperature (100%). The evaluation was carried out on the basis of the integrated intensities of the δH_2O band in the IR spectra (see figure S6).

As shown in Figure 6, ca. 80% of water was desorbed from both materials by outgassing at 373 K. The complete dehydration of HA–2 was then attained by increasing the outgassing temperature to 433 K, whereas after such treatment HA–1 still retained ca. 10% of the initial amount of H_2O molecules, which were completely desorbed at 573 K. This outcome suggests several differences in the surface structure of the two types of HA nanoparticles.

The full sets of spectra collected at decreasing CO coverage for HA–1 and HA–2 materials pre-outgassed at 433 K are shown in Figure 7 A, B), while those related to materials pre-outgassed at 573 K are reported in Figure S7 in the SI).

(remaining part of the page left intentionally blank,

in order Figure 7 and related caption appear in the same page)

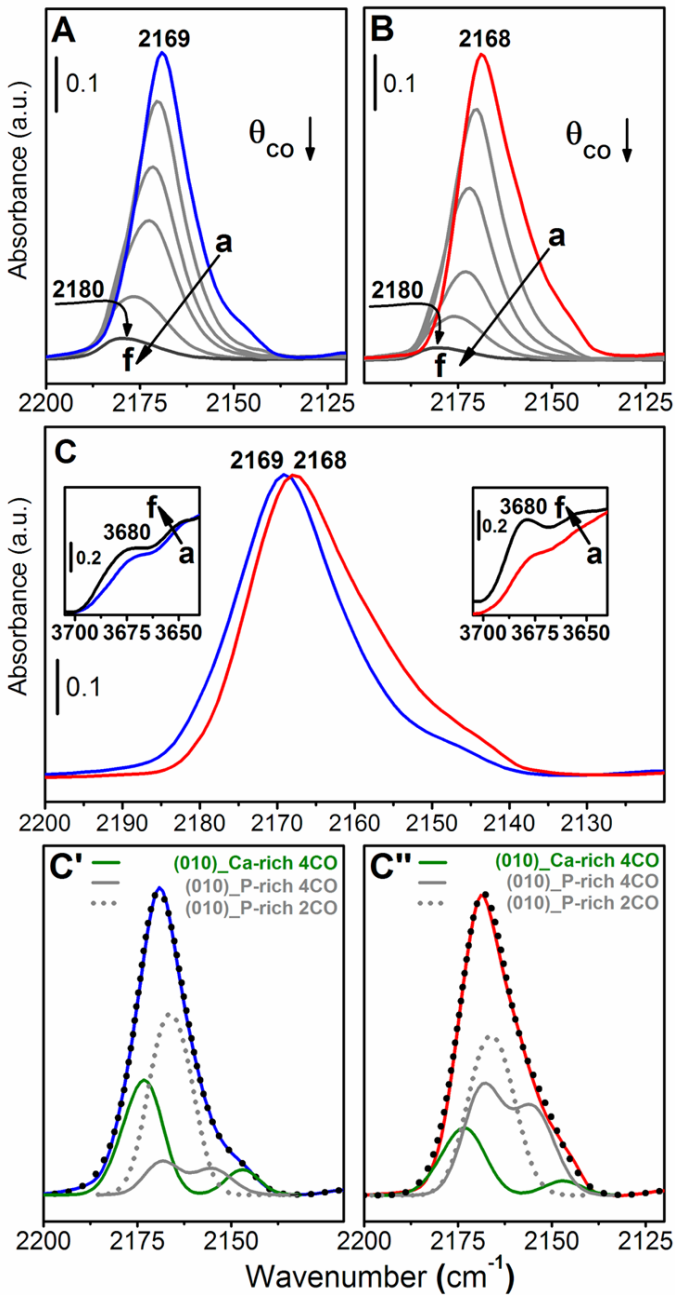

Figure 7. IR spectra of CO adsorbed at ca. 100 K on A) HA–1 and B) HA–2, both pre-outgassed at 433 K. The lettering is in the sense of decreasing CO pressure, from (a) 25 mbar to (f) outgassing for 1 min. Spectra are reported after subtraction of the spectrum of the material before CO adsorption. Panel C: spectra at maximum CO coverage of HA–1 (blue curve) and HA–2 (red-curve), the same as curves "a" in both A and B panels. In the insets are the original spectra in the 3680-3625 cm^{-1} region (left: HA–1, right: HA–2) of: (a) in contact with 25 mbar CO and (f) after CO outgassing.

Panels C',C'': blue and red solid lines are the experimental spectra (the same as in section C), while all the other curves represent B3LYP spectra calculated on the basis of the method reported in ref.[24] Green curves: spectra of 4 CO molecules adsorbed on (010)_Ca-rich surface; solid grey spectra: B3LYP spectra of 4 CO molecules adsorbed on (010)_P-rich surface; dotted grey spectra: B3LYP spectra of 2 CO molecules adsorbed on (010)_P-rich; in each panel, the sum of the B3LYP spectra resulted in the black-dotted spectrum.

In both cases, a broad band, initially located at ca. 2168/2169 cm^{-1} and then shifting, while decreasing in intensity, to ca. 2180 cm^{-1}, was observed, which was related to CO molecules adsorbed on surface Ca^{2+} cations.[14, 25] Recent findings indicated that the evolution of the νCO band by changing the CO coverage is not simply due to a change in the amount of adsorbed monocarbonyls per Ca_{surf}^{2+}, but to the conversion among Ca_{surf}^{2+}-(CO)n adducts, with "n" ranging from 1 to 4.[24] Noticeably, Ca_{surf}^{2+}-CO monocarbonyls exhibited almost the same calculated νCO frequency for {001} and (010)R, (010)_Ca-rich and (010)_P-rich terminations (see Figure S8), whereas differences appeared among the calculated νCO patterns of Ca_{surf}^{2+}–$(CO)_n$ carbonyls on such surfaces for n=2–4 (ref.[24] and Figure S8 in the SI). Indeed, the spectra collected at maximum CO coverage for both HA materials exhibited some difference in position and shape. In addition to calcium cations, surface P-OH can also act as adsorption centers for CO, producing an IR band at ca. 2170 cm^{-1}.[61] Indeed, a weak band at ca. 3680 cm^{-1} monitored the presence of such P-OH groups at the surface of both HA–1 and HA–2 (curves f in the insets of panel C). This signal decreased in intensity when CO was admitted to the sample (curves a in the insets of panel C), indicating their interaction with probe molecules. As a consequence of this interaction, the νOH signal due to P-OH was downshifted to 3590 cm^{-1} (Figure S9 in the SI), with a $\Delta\nu$ = 90 cm^{-1} probing that these groups should exhibit a weak acidity._ENREF_30[27] Nevertheless, an evaluation based on literature data[61] of the ratio between the integrated intensity of the νOH band of unperturbed P-OH and that expected for the stretching band of CO adsorbed on them suggested that the latter should contribute for a negligible part of the νCO signal observed when dosing the probe molecules on both HA–1 and HA–2 (displayed in panel C as the simulated shadowed components). However, it must be considered that the relative amount of hydroxyl groups with respect to surface cations, as revealed by CO adsorption, can change significantly depending on the preparation method.[62]

To understand the nature of the difference in the νCO profiles, the method established in ref.[24] was exploited, fitting the spectrum at high CO coverage with a weighted linear combination of the

calculated B3LYP spectra for all Ca_{surf}^{2+}-(CO)n adducts (n=1-4) on (001), (010)R, (010)_Ca-rich and (010)_P-rich surfaces which are shown in Figure S8. To elucidate the relative importance of the considered cases in an unbiased manner, the procedure was initiated by setting all the weights to unity. After the refinement, only the spectra of Ca_{surf}^{2+}–(CO)n adducts on {010}_Ca–rich with n=3, 4 and on {010}_P–rich surfaces with n=4, 2 exhibited a ratio of different weights significantly different from zero (C',C''). The values of the ratio between {010}_Ca–rich and {010}_P–rich surfaces found for the two materials are listed in Table 5. The most striking feature is the difference in the Ca-rich: P-rich ratio exhibited by HA–1 and HA–2 pre-outgassed at 433 K (ca. 1:1.4 and 1:5.0, respectively). This result indicated that the presence of acetate anions during the preparation of HA nanoparticles affects the formation of {010} facets, favoring the terminations of {010}_P–rich type. Moreover, the {010}_Ca–rich:{010}_P–rich ratio exhibited a significant evolution for HA–2 pre-outgassed at 573 K, becoming equivalent to what obtained for HA–1 (ca. 1:1.7 and 1: 1.8, respectively), which, conversely, exhibited a limited modification after such treatment. This evolution exhibited the same trend as the SSA of the materials when outgassed at 573 K, which decreased significantly in the case of HA–2 and only to a slight extent for HA–1 (see Table 1). Considering that TEM observations indicated that such a decrease should result from an agglomeration of HA–2 nanoparticles, the combination of SSA and IR spectra of adsorbed CO suggests that the treatment at 573 K of these HA nanoparticles resulted in a preferential stacking among {010}_P–rich facets.

Table 5. Relative ratio of (010)_Ca-rich surfaces towards (010)_P-rich as revealed by the analysis of the IR spectra of adsorbed CO

	(010)_Ca-rich : (010)_P-rich	
	Pre-outgassing temperature:	
	433 K	**573 K**
HA–1	1.00±0.04 : 1.40±0.06	1.00±0.09 : 1.80±0.13
HA–2	1.00±0.05 : 5.05±0.18	1.00±0.03 : 1.74±0.04

4. CONCLUSIONS

The collection of data obtained in this work allows us to conclude that the presence of acetate ions in the reaction media significantly influences the formation of hydroxyapatite nanoparticles, in terms of size and surface structure. Indeed, nanoparticles appeared shorter along the c-axis with respect to HA nanoparticles produced in the absence of CH_3COO^-, indicating that these species might stabilize {001} facets during particle growth. Moreover, {010} facets remained the most abundant for HA nanoparticles prepared in the presence of acetates, but, once synthesized in the absence of CH_3COO^- groups, their surfaces appeared to be definitely enriched in {010}_P–rich terminations with respect to the {010}_Ca–rich. Apparently, such terminations are preferential surfaces for stacking during particle aggregation promoted by thermal treatment. Hence, this work indicated that the use of calcium chelating agents during the synthesis of HA nanoparticles for different biomedical applications is an effective approach to tailor size and surface structural features.

Finally, from a methodological point of view, it is notable that the synergy between the use of HR-TEM and IR spectra of adsorbed CO resulted in a significant added value, allowing the recognition of differences in the actual terminations of nanoparticle facets of the same crystallographic type.

ASSOCIATED CONTENT

Supporting Information

(1) XRD patterns and (2) TEM images of HA−1, HA−2 outgassed at 573K, (3) IR spectra of HA−1, exchanged with D_2O and then outgassed at b.t., (4) TGA curves of HA−1 and HA−2; (5) example of data elaboration for the extraction of the signals due to adsorbed H_2O, (6) IR spectra of HA−1 and HA−2 in the νOH, δH_2O regions, (7) IR spectra of adsorbed CO on HA−1 and HA−2 and related profile analysis, (8) B3LYP spectra of CO adsorbed on (001) and {010} HA surfaces, 9) IR spectra, in the high frequency region, of HA−2 in contact at 100 K with 25 mbar CO and after CO outgassing

AUTHOR INFORMATION

Corresponding Authors

* E-mail: gianmario.martra@unito.it; sakhnoyura@alice.it

phone: +39-011 670 7536/7538; fax: +39-011 670 7855

Notes

The authors declare no competing financial interest.

ACKNOWLEDGMENTS

This research has been carried out in the frame of the project “Advances in nanostructured materials and interfaces for key technologies” (Progetto di Ricerca di Ateneo – Compagnia di San Paolo – 2011 – Linea 1A, progetto ORTO11RRT5). MI and AT acknowledge the PNR-CNR Aging Program 2012-2014 and the Flagship Project NanoMAX (PNR-CNR 2011-2013). Authors acknowledge Prof. Piero Ugliengo and Dr. Fabio Chiatti (University of Torino) for fruitful discussions and for providing theoretical B3LYP spectra. Dr. Luca Bertinetti and Mr. Marco Fabbiani are acknowledged for support for TEM observation of HA-1 and statistical data analysis, respectively.

REFERENCES

1. Dorozhkin, S. V. Calcium Orthophosphates in Nature, Biology and Medicine. *Materials* **2009**, *2*, 399-498.
2. Roveri, N.; Palazzo, B. *Nanotechnologies for the Life Sciences*; Wiley-VCH, Weinheim, Germany, 2006.
3. Jones, F. H. Teeth and Bones: Applications of Surface Science to Dental Materials and Related Biomaterials. *Surf. Sci. Rep.* **2001**, *42*, 79-205.
4. Webster, T. J.; Siegel, R. W.; Bizios, R. Osteoblast Adhesion on Nanophase Ceramics. *Biomaterials* **1999**, *20*, 1221-1227.
5. Castner, D. G.; Ratner, B. D. Biomedical Surface Science: Foundations to Frontiers. *Surf. Sci.* **2002**, *500*, 28-60.
6. Kasemo, B. Biological Surface Science. *Surf. Sci.* **2002**, *500*, 656-677.
7. Tirrell, M.; Kokkoli, E.; Biesalski, M. The Role of Surface Science in Bioengineered Materials. *Surf. Sci.* **2002**, *500*, 61-83.
8. Iafisco, M., et al. Smart Delivery of Antitumoral Platinum Complexes from Biomimetic Hydroxyapatite Nanocrystals. *J. Mater. Chem.* **2009**, *19*, 8385-8392.
9. Xu, Z.; Liu, C.; Wei, J.; Sun, J. Effects of Four Types of Hydroxyapatite Nanoparticles with Different Nanocrystal Morphologies and Sizes on Apoptosis in Rat Osteoblasts. *J. Appl. Toxicol.* **2012**, *32*, 429-35.
10. Yao, X.; Yao, H. W.; Li, G. Y.; Li, Y. T. Biomimetic Synthesis of Needle-Like Nano-Hydroxyapatite Templated by Double-Hydrophilic Block Copolymer. *J. Mater. Sci.* **2010**, *45*, 1930-1936.
11. Shuai, C. J.; Feng, P.; Nie, Y.; Hu, H. L.; Liu, J. L.; Peng, S. P. Nano-Hydroxyapatite Improves the Properties of Beta-Tricalcium Phosphate Bone Scaffolds. *Int. J. Appl. Ceram. Technol.* **2013**, *10*, 1003-1013.
12. Deng, Y.; Wang, H. N.; Zhang, L.; Li, Y. B.; Wei, S. C. In Situ Synthesis and in Vitro Biocompatibility of Needle-Like Nano-Hydroxyapatite in Agar-Gelatin Co-Hydrogel. *Mater. Lett.* **2013**, *104*, 8-12.
13. a) Ito, H.; Oaki, Y.; Imai, H. Selective Synthesis of Various Nanoscale Morphologies of Hydroxyapatite Via an Intermediate Phase. *Cryst. Growth Des.* **2008**, *8*, 1055-1059; b) Kobayashi, T.; Ono, S.; Hirakura, S.; Oaki, Y.; Imai, H. Morphological Variation of Hydroxyapatite Grown in Aqueous Solution Based on Simulated Body Fluid. *CrystEngComm* **2012**, *14*, 1143-1149.
14. a) Bertinetti, L.; Tampieri, A.; Landi, E.; Ducati, C.; Midgley, P. A.; Coluccia, S.; Martra, G. Surface Structure, Hydration, and Cationic Sites of Nanohydroxyapatite: Uhr-Tem, Ir, and Microgravimetric Studies. *J. Phys. Chem. C* **2007**, *111*, 4027-4035; b) Sakhno, Y.; Bertinetti, L.; Iafisco, M.; Tampieri, A.; Roveri, N. Surface Hydration and Cationic Sites of Nanohydroxyapatites with Amorphous or Crystalline Surfaces: A Comparative Study. *J. Phys. Chem. C*, **2010**, *114*, 16640-16648.
15. Eppell, S. J.; Tong, W. D.; Katz, J. L.; Kuhn, L.; Glimcher, M. J. Shape and Size of Isolated Bone Mineralites Measured Using Atomic Force Microscopy. *J. Orthop. Res.* **2001**, *19*, 1027-1034.
16. Fratzl, P.; Gupta, H. S.; Paschalis, E. P.; Roschger, P. Structure and Mechanical Quality of the Collagen-Mineral Nano-Composite in Bone. *J. Mater. Chem.* **2004**, *14*, 2115-2123.
17. Olszta, M. J.; Cheng, X. G.; Jee, S. S.; Kumar, R.; Kim, Y. Y.; Kaufman, M. J.; Douglas, E. P.; Gower, L. B. Bone Structure and Formation: A New Perspective. *Mater. Sci. Eng., R* **2007**, *58*, 77-116.
18. Delgado-Lopez, J. M.; Frison, R.; Cervellino, A.; Gomez-Morales, J.; Guagliardi, A.; Masciocchi, N. Crystal Size, Morphology, and Growth Mechanism in Bio-Inspired Apatite Nanocrystals. *Adv. Funct. Mater.* **2014**, *24*, 1090-1099.

19. Kandori, K.; Fudo, A.; Ishikawa, T. Study on the Particle Texture Dependence of Protein Adsorption by Using Synthetic Micrometer-Sized Calcium Hydroxyapatite Particles. *Colloids Surf., B* **2002**, *24*, 145-153.
20. Sato, K.; Kogure, T.; Iwai, H.; Tanaka, J. Atomic-Scale {1010} Interfacial Structure in Hydroxyapatite Determined by High-Resolution Transmission Electron Microscopy. *J. Am. Ceram. Soc.* **2002**, *85*, 3054-3058.
21. Ospina, C. A.; Terra, J.; Ramirez, A. J.; Farina, M.; Ellis, D. E.; Rossi, A. M. Experimental Evidence and Structural Modeling of Nonstoichiometric (010) Surfaces Coexisting in Hydroxyapatite Nano-Crystals. *Colloids Surf., B* **2012**, *89*, 15-22.
22. Astala, R.; Stottt, M. J. First-Principles Study of Hydroxyapatite Surfaces and Water Adsorption. *Phys. Rev. B: Condens. Matter Mater. Phys.* **2008**, *78*.
23. Corno, M.; Rimola, A.; Bolis, V.; Ugliengo, P. Hydroxyapatite as a Key Biomaterial: Quantum-Mechanical Simulation of Its Surfaces in Interaction with Biomolecules. *Phys. Chem. Chem. Phys.* **2010**, *12*, 6309-6329.
24. Chiatti, F.; Corno, M.; Sakhno, Y.; Martra, G.; Ugliengo, P. Revealing Hydroxyapatite Nanoparticle Surface Structure by CO Adsorption: A Combined B3LYP and Infrared Study. *J. Phys. Chem. C* **2013**, *117*, 25526-25534.
25. Pekounov, Y.; Chakarova, K.; Hadjiivanov, K. Surface Acidity of Calcium Phosphate and Calcium Hydroxyapatite: FTIR Spectroscopic Study of Low-Temperature CO Adsorption. *Mater. Sci. Eng., C* **2009**, *29*, 1178-1181.
26. Diallo-Garcia, S.; Laurencin, D.; Krafft, J. M.; Casale, S.; Smith, M. E.; Lauron-Pernot, H.; Costentin, G. Influence of Magnesium Substitution on the Basic Properties of Hydroxyapatites. *J. Phys. Chem. C* **2011**, *115*, 24317-24327.
27. Diallo-Garcia, S.; Ben Osman, M.; Krafft, J. M.; Boujday, S.; Guylene, C. Discrimination of Infrared Fingerprints of Bulk and Surface POH and OH of Hydroxyapatites. *Catal. Today* **2014**, *226*, 81-88.
28. Liou, S. C.; Chen, S. Y.; Lee, H. Y.; Bow, J. S. Structural Characterization of Nano-Sized Calcium Deficient Apatite Powders. *Biomaterials* **2004**, *25*, 189-196.
29. a) Dorozhkin, S. V. Nanosized and Nanocrystalline Calcium Orthophosphates. *Acta Biomater.* **2010**, *6*, 715-734; b) Swain, S. K.; Dorozhkin, S. V.; Sarkar, D. Synthesis and dispersion of hydroxyapatite nanopowders. *Mater. Sci. Eng., C* **2012**, *32*, 1237-1240.
30. Barralet, J. E.; Tremayne, M.; Lilley, K. J.; Gbureck, U. Modification of Calcium Phosphate Cement with Alpha-Hydroxy Acids and Their Salts. *Chem. Mater.* **2005**, *17*, 1313-1319.
31. Qiu, H.; Yang, J.; Kodali, P.; Koh, J.; Ameer, G. A. A Citric Acid-Based Hydroxyapatite Composite for Orthopedic Implants. *Biomaterials* **2006**, *27*, 5845-5854.
32. Ikawa, N.; Kimura, T.; Oumi, Y.; Sano, T. Amino Acid Containing Amorphous Calcium Phosphates and the Rapid Transformation into Apatite. *J. Mater. Chem.* **2009**, *19*, 4906-4913.
33. Achelhi, K.; Masse, S.; Laurent, G.; Saoiabi, A.; Laghzizil, A.; Coradin, T. Role of Carboxylate Chelating Agents on the Chemical, Structural and Textural Properties of Hydroxyapatite. *Dalton Trans.* **2010**, *39*, 10644-10651.
34. Delgado-Lopez, J. M.; Iafisco, M.; Rodriguez, I.; Tampieri, A.; Prat, M.; Gomez-Morales, J. Crystallization of Bioinspired Citrate-Functionalized Nanoapatite with Tailored Carbonate Content. *Acta Biomater.* **2012**, *8*, 3491-3499.
35. Boskey, A. L. Osteopontin and Related Phosphorylated Sialoproteins: Effects on Mineralization. *Ann. N. Y. Acad. Sci.* **1995**, *760*, 249-256.
36. Harris, N. L.; Rattray, K. R.; Tye, C. E.; Underhill, T. M.; Somerman, M. J.; D'Errico, J. A.; Chambers, A. F.; Hunter, G. K.; Goldberg, H. A. Functional Analysis of Bone Sialoprotein: Identification of the Hydroxyapatite-Nucleating and Cell-Binding Domains by Recombinant Peptide Expression and Site-Directed Mutagenesis. *Bone* **2000**, *27*, 795-802.

37. Gericke, A.; Qin, C.; Spevak, L.; Fujimoto, Y.; Butler, W. T.; Sorensen, E. S.; Boskey, A. L. Importance of Phosphorylation for Osteopontin Regulation of Biomineralization. *Calcif. Tissue Int.* **2005**, *77*, 45-54.
38. Hu, Y. Y.; Rawal, A.; Schmidt-Rohr, K. Strongly Bound Citrate Stabilizes the Apatite Nanocrystals in Bone. *Proc. Natl. Acad. Sci. U. S. A.* **2010**, *107*, 22425-22429.
39. Xie, B. Q.; Nancollas, G. H. How to Control the Size and Morphology of Apatite Nanocrystals in Bone. *Proc. Natl. Acad. Sci. U. S. A.* **2010**, *107*, 22369-22370.
40. Lopez-Macipe, A.; Gomez-Morales, J.; Rodriguez-Clemente, R. Nanosized Hydroxyapatite Precipitation from Homogeneous Calcium/Citrate/Phosphate Solutions Using Microwave and Conventional Heating. *Adv. Mater.* **1998**, *10*, 49-53.
41. Pan, H. H.; Tao, J. H.; Xu, X. R.; Tang, R. K. Adsorption Processes of Gly and Glu Amino Acids on Hydroxyapatite Surfaces at the Atomic Level. *Langmuir* **2007**, *23*, 8972-8981.
42. a) Koutsopoulos, S.; Dalas, E. Hydroxyapatite Crystallization in the Presence of Serine, Tyrosine and Hydroxyproline Amino Acids with Polar Side Groups. *J. Cryst. Growth* **2000**, *216*, 443-449; b) Koutsopoulos, S.; Dalas, E. Hydroxyapatite Crystallization in the Presence of Amino Acids with Uncharged Polar Side Groups: Glycine, Cysteine, Cystine and Glutamine *Langmuir* **2001**, *17*, 1074-1079; c) Koutsopoulos, S.; Dalas, E. The Crystallization of Hydroxyapatite in the Presence of Lysine *J. Colloid Interface Sci.* **2000**, *231*, 207-212.
43. Gonzalez-McQuire, R.; Chane-Ching, J. Y.; Vignaud, E.; Lebugle, A.; Mann, S. Synthesis and Characterization of Amino Acid-Functionalized Hydroxyapatite Nanorods. *J. Mater. Chem.* **2004**, *14*, 2277-2281.
44. Lee, W. H.; Loo, C. Y.; Van, K. L.; Zavgorodniy, A. V.; Rohanizadeh, R. Modulating Protein Adsorption onto Hydroxyapatite Particles Using Different Amino Acid Treatments. *J. R. Soc., Interface* **2012**, *9*, 918-927.
45. Xu, Z.; Yang, Y.; Wang, Z.; Mkhonto, D.; Shang, C.; Liu, Z. P.; Cui, Q.; Sahai, N. Small Molecule-Mediated Control of Hydroxyapatite Growth: Free Energy Calculations Benchmarked to Density Functional Theory. *J. Comput. Chem.* **2014**, *35*, 70-81.
46. Tõnsuaadu, K.; Gross, K. A.; Plūduma, L.; Veiderma, V. A Review on the Thermal Stability of Calcium Apatites. *J. Therm. Anal. Calorim.* **2011**, *110*, 647-659.
47. Landi, E.; Celotti, G.; Logroscino, G.; Tampieri, A. Carbonated Hydroxyapatite as Bone Substitute. *J. Eur. Ceram. Soc.* **2003**, *23*, 2931-2937.
48. Meldrum, A.; Wang, L. M.; Ewing, R. C. Electron-Irradiation-Induced Phase Segregation in Crystalline and Amorphous Apatite: A TEM Study. *Am. Mineral.* **1997**, *82*, 858-869.
49. Wang, L. M.; Wang, S. X.; Ewing, R. C.; Meldrum, A.; Birtcher, R. C.; Provencio, P. N.; Weber, W. J.; Matzke, H. Irradiation-Induced Nanostructures. *J. Mater. Sci. Eng. A* **2000**, *286*, 72-80.
50. Williams, D. B.; Barry Carter, C. *Transmission Electron Microscopy: A Textbook for Materials Science* Springer, New York, 2009.
51. Puvvada, N.; Panigrahi, P. K.; Pathak, A. Room Temperature Synthesis of Highly Hemocompatible Hydroxyapatite, Study of Their Physical Properties and Spectroscopic Correlation of Particle Size. *Nanoscale* **2010**, *2*, 2631-2638.
52. Cazalbou, S.; Combes, C.; Eichert, D.; Rey, C. Adaptative Physico-Chemistry of Bio-Related Calcium Phosphates. *J. Mater. Chem.* **2004**, *14*, 2148-2153.
53. Nakamoto, K. *Infrared and Raman Spectra of Inorganic and Coordination Compounds*; Wiley, New York, U.S., 1986.
54. a) Fleet, M. E. Infrared Spectra of Carbonate Apatites: V2-Region Bands. *Biomaterials* **2009**, *30*, 1473-1481; b) Fleet, M. E.; Liu, X. Y.; King, P. L. Accommodation of the Carbonate Ion in Apatite: An FTIR and X-Ray Structure Study of Crystals Synthesized at 2-4 Gpa. *Am. Mineral.* **2004**, *89*, 1422-1432.
55. a) LeGeros, R. Z.; LeGeros, J. P.; Trautz, O. R.; Klein, E. Spectral Properties of Carbonate in Carbonate-Containing Apatites. *Dev. Appl. Spectrosc.* **1970**, *7B*, 3-12; b) LeGeros, R. Z.; Trautz,

O. R.; Klein, E.; LeGeros, J. P. Two Types of Carbonate Substitution in the Apatite Structure. *Experientia* **1969**, *25*, 5-7.
56. Rheman, I.; Bonfield, W. *J. Mater. Sci.: Mater. Med.* **1997**, *8*, 1-4.
57. a) Elliott, J. C. *The Interpretation of the Infra-Red Absorption Spectra of Some Carbonate-Containing Apatites.*; John Wright & Sons, Bristol, UK, 1964; b) Elliott, J. C. *Tooth Enamel: Its Composition, Properties, and Fundamental Structure*; Williams and Wilkins Co, London, 1965.
58. Bonel, G. Contribution À L'étude De La Carbonatation Des Apatites. I. Synthèse Et Étude Des Propriétés Physico-Chimiques Des Apatites Carbonateées Du Type A. *Ann. Chim.* **1972**, *7*, 65-88.
59. Bolis, V.; Busco, C.; Martra, G.; Bertinetti, L.; Sakhno, Y.; Ugliengo, P.; Chiatti, F.; Corno, M.; Roveri, N. Coordination Chemistry of Ca Sites at the Surface of Nanosized Hydroxyapatite: Interaction with H_2O and CO. *Philos. Trans. R. Soc., A* **2011**, *370*, 1313-1336.
60. Corno, M.; Busco, C.; Bolis, V.; Tosoni, S.; Ugliengo, P. Water Adsorption on the Stoichiometric (001) and (010) Surfaces of Hydroxyapatite: A Periodic B3LYP Study. *Langmuir* **2009**, *25*, 2188-2198.
61. Gianotti, E.; Oliveira, E. C.; Coluccia, S.; Pastore, H. O.; Marchese, L. The Surface Acidity of Mesoporous Silicoaluminophosphates: A FTIR Study. *Stud. Surf. Sci. Catal.* **2004**, *154*, 1498-1504.
62. Diallo-Garcia, S.; Ben Osman, M.; Krafft, J. M.; Casale, S.; Thomas, C.; Kubo, J.; Costentin, G. Identification of Surface Basic Sites and Acid-Base Pairs of Hydroxyapatite. *J. Phys. Chem. C* **2014**, *118*, 12744-12757.